

A community benchmark for 2-D Cartesian compressible convection in the Earth's mantle

Scott D. King,¹ Changyeol Lee,¹ Peter E. van Keken,² Wei Leng,³ Shijie Zhong,³ Eh Tan,⁴ Nicola Tosi^{5,6} and Masanori C. Kameyama⁷

¹Department of Geosciences, Virginia Tech, Blacksburg, VA 24061, USA. E-mail: sdk@vt.edu

²Department of Geological Sciences, University of Michigan, Ann Arbor, MI 48109, USA

³Department of Physics, University of Colorado, Boulder, CO 80309, USA

⁴Seismological Laboratory, Caltech, Pasadena, CA 91125, USA

⁵Department of Geophysics, Faculty of Mathematics and Physics, Charles University, Prague, Czech Republic

⁶Institute of Geological Sciences, Freie Universität, Berlin, Germany

⁷Geodynamics Research Center (GRC), Ehime University, Matsuyama, Japan

Accepted 2009 October 8. Received 2009 October 5; in original form 2009 June 19

SUMMARY

Benchmark comparisons are an essential tool to verify the accuracy and validity of computational approaches to mantle convection. Six 2-D Cartesian compressible convection codes are compared for **steady-state constant and temperature-dependent viscosity** cases as well as **time-dependent constant viscosity** cases. In general we find good agreement between all codes when comparing average flow characteristics such as Nusselt number and rms velocity. At Rayleigh numbers near 10^6 and dissipation numbers between 0 and 2, the results differ by approximately 1 per cent. Differences in discretization and use of finite volumes versus finite elements dominate the differences. There is a small systematic difference between the use of the anelastic liquid approximation (ALA) compared to that of the truncated ALA. In determining the onset of time-dependence, there was less agreement between the codes with a spread in the Rayleigh number where the first bifurcation occurs ranging from 7.79×10^5 to 1.05×10^6 .

Key words: Numerical solutions; Numerical approximations and analysis; Equations of state; Dynamics of lithosphere and mantle.

1 INTRODUCTION

As pressure increases through the mantle there is a corresponding increase in density due to self-compression. In a vigorously convecting mantle, the rate at which mechanical energy is converted into heat (i.e. viscous dissipation) is non-negligible and contributes to the heat energy of the fluid, resulting in adiabatic temperature and density gradients that reduce the vigour of convection. In the non-dimensional form of the equations, the magnitude of the dissipation is controlled by a dimensionless parameter called the **Dissipation number, Df** . For the Earth's mantle, the effect of compressibility is moderate (Jarvis & McKenzie 1980) and the dissipation number is between 0.25 and 0.8. The majority of mantle convection studies have assumed an incompressible mantle where the dissipation number is assumed to be zero. However, viscous dissipation may interact with rheology and/or changes in composition and the effect on mantle dynamics and geophysical observations may be more significant than has been previously thought (e.g. King & Ita 1995; Ita & King 1998; Tan & Gurnis 2005, 2007; Leng & Zhong 2008; Lee & King 2009). In addition, the effect of compressibility on time-dependent flow has not been examined. Often an adiabatic gradient is added *a posteriori* to convection calculations to incorporate the

effect of compressibility. However, this does not take into account the potential feedback between rheology and adiabatic heating (*cf.* Yuen *et al.* 1987). While there has been extensive benchmarking of incompressible mantle convection codes (Blankenbach *et al.* 1989; Travis *et al.* 1990; van Keken *et al.* 1997; Koglin *et al.* 2005; van Keken *et al.* 2008), there has been no compressible convection benchmark.

This paper grew out of a workshop on compressible convection held at Purdue University in 2006 March that was sponsored by the Computational Infrastructure for Geodynamics project (www.geodynamics.org). As in Blankenbach *et al.* (1989) we focus on a **comparison of derived quantities** from the temperature and velocity field that are predicted for a number of prescribed cases. **The derived quantities include the Nusselt number Nu (non-dimensional average heat flow), and the non-dimensional root-mean-square (rms) velocity, volume averaged work and viscous dissipation.** We did not compare computational efficiency given the different computer architectures that the contributing groups employed. Authors chose the grid resolution based on their experience with the codes and their desire to balance accuracy versus CPU time. We illustrate the effect of increasing grid resolution on one typical problem with one code. Many of the codes have previously

published resolution analyses for Bousinessq convection (e.g. van Keken *et al.* 1997; Tan & Gurnis 2007; Leng & Zhong 2008; King 2009). The benchmark cases formulated below result in convective vigour that is below that of the Earth's interior as expressed in the Nusselt number (well below the 20–30 estimated for the Earth).

The cases are also for isoviscous or limited temperature-dependent viscosity and for 2-D Cartesian geometry. While simplified, the benchmark cases provide a basis for a comparison between multiple codes that can be performed without the need for massively parallel computing. We hope that this benchmark comparison will stimulate the further development of a benchmark in 3-D spherical geometry at appropriate convective vigour.

In the Section 2, we outline the equations and different approximations for compressible convection. In Section 3, the benchmark problems are described and, Section 4 describes the six codes used in the benchmark. Section 5 describes the benchmark results. We chose a limited, representative number of experiments for the figures illustrating the difference between results from the different codes and, we include tables of results from all experiments in an online supplement.

2 EQUATIONS

While the general, dimensional equations for a compressible fluid and various simplifying approximations have been presented elsewhere (e.g. Turcotte *et al.* 1974; Jarvis & McKenzie 1980; Ita & King 1994; Schubert *et al.* 2001; Leng & Zhong 2008), it is worth repeating them here again for clarity. The derivation below follows that in Schubert *et al.* (2001). Mass conservation is given by

$$\frac{\partial \rho}{\partial t} + \nabla \cdot (\rho \vec{u}) = 0, \quad (1)$$

where ρ is the density and \vec{u} is the velocity. The conservation of momentum is given by,

$$\frac{D\rho \vec{u}}{Dt} = -\nabla P + \nabla \cdot \tau + \rho \vec{g}, \quad (2)$$

where P is the pressure, \vec{g} is the gravity, D/Dt is the material derivative, and τ is the deviatoric stress tensor given by,

$$\tau = 2\eta \dot{\epsilon} = \eta(\nabla \vec{u} + \nabla \vec{u}^T) - \frac{2}{3}\eta \nabla \cdot \vec{u} \delta_{ij}, \quad (3)$$

where η is the dynamic viscosity, $\dot{\epsilon}$ is the strain-rate tensor, and δ_{ij} is the Kroneker delta. Eq. (3) assumes that the bulk viscosity of the fluid is zero. Finally, the equation of energy conservation is given by,

$$\rho c_p \frac{DT}{Dt} - \alpha T \frac{DP}{Dt} = \nabla \cdot (k \nabla T) + \rho H + \phi, \quad (4)$$

where T is the temperature, c_p is the heat capacity at constant pressure, α is the coefficient of thermal expansion, k is the thermal conductivity, H is the volumetric heat production and ϕ is the viscous dissipation given by,

$$\phi = \frac{1}{2} \tau : \dot{\epsilon} = \tau_{ij} \frac{\partial u_i}{\partial x_j}. \quad (5)$$

In compressible convection, there is the additional required assumption—the reference state,

$$T = \bar{T} + T' \quad (6)$$

$$P = \bar{p} + p' \quad (7)$$

$$\rho = \bar{\rho}(\bar{T}, \bar{p}) + \rho', \quad (8)$$

where the overbarred quantities are time-independent and functions of depth only. The reference pressure is given by the hydrostatic approximation,

$$\nabla \bar{p} = \bar{\rho} g. \quad (9)$$

Using the assumption that $p' \ll \bar{p}$, we can eliminate pressure from the energy eq. (4), yielding

$$\rho c_p \frac{DT'}{Dt} = \nabla \cdot [k \nabla (T' + \bar{T})] + \rho H + \phi - \rho c_p \vec{u} \cdot \nabla \bar{T} - \alpha(\bar{T} + T') \bar{\rho} g w, \quad (10)$$

where $\vec{u} \cdot \vec{g} = -wg$, where w is the upward component of velocity.

For the reference state (\bar{p}, \bar{T}) , we assume an adiabatic Adams–Williamson equation of state (Birch 1952), where

$$\bar{\rho}(z) = \rho_r \exp\left(\frac{\alpha_r g_r}{\gamma_r c_{pr}} z\right), \quad \bar{T}(z) = T_{\text{surf}} \exp\left(\frac{\alpha_r g_r}{c_{pr}} z\right), \quad (11)$$

where z is the depth coordinate (parallel to the direction of gravity), γ_r is the reference value for the Grüneisen parameter, T_{surf} is the surface temperature, and variables with the subscript r are constant values used in defining the reference state. From this reference state, we note that $\nabla \bar{T} = (0, -\alpha_r g_r \bar{T}/c_{pr})$, which along with dropping terms with ρ' and that $c_p \approx c_{pr}$, allows us to further simplify the energy eq. (10),

$$\bar{\rho} \bar{c}_{pr} \frac{DT'}{Dt} = \nabla \cdot [k \nabla (T' + \bar{T})] + \bar{\rho} H + \phi - \bar{\rho} \bar{\alpha} g w T'. \quad (12)$$

The expansivity $\bar{\alpha}$ is $\frac{\alpha}{\alpha_r}$ and formally dependent on the reference state. For the purposes of the benchmark we will assume that $\bar{\alpha} = 1$.

2.1 Equations under the anelastic liquid approximation (ALA)

We non-dimensionalize the equations using the reference values for density, ρ_r , thermal expansivity, α_r , temperature contrast, ΔT_r , thermal conductivity, k_r , heat capacity, c_p , once again assuming that $c_p \approx c_{pr}$ depth of the fluid layer, L and viscosity, η_r . The non-dimensionalization for velocity, u_r , pressure, p_r and time, t_r , become

$$u_r = \frac{k_r}{\rho_r c_p L}, \quad p_r = \frac{\eta_r k_r}{\rho_r c_p L^2}, \quad t_r = \frac{\rho_r c_p L^2}{k_r}. \quad (13)$$

The non-dimensionalization introduces four non-dimensional numbers, the Prandtl number, Pr , the Mach number, M , the dissipation number, Di and the Rayleigh number, Ra . If we assume that the relative volume change due to temperature, $\alpha_r \Delta T_r \ll 1$, $M^2 Pr \ll 1$ and $Pr \rightarrow \infty$, we arrive at the ALA.

Under the ALA, the conservation of mass becomes,

$$\nabla \cdot (\bar{\rho} \vec{u}) = 0, \quad (14)$$

the conservation of momentum becomes,

$$0 = -\nabla p' + \nabla \cdot \tau + Di \frac{\bar{\rho} c_p \hat{g}}{K_s \gamma_r c_v} p' - Ra \bar{\rho} \bar{\alpha} \hat{g} T' / \Delta T_r, \quad (15)$$

where \hat{g} is the unit vector in the direction of gravity, c_v is the specific heat at constant volume, $\bar{\rho}$ is now dimensionless [i.e. eq. (11) divided by ρ_r] and the Rayleigh number and dissipation number are given by

$$Ra = \frac{\alpha_r \Delta T_r \rho_r^2 g_r L^3 c_p}{\eta_r k_r}, \quad Di = \frac{\alpha_r g_r L}{c_p}. \quad (16)$$

With the assumption of constant thermal conductivity, and using the dimensionless reference states for $\bar{\rho}$ and \bar{T} given by

$$\bar{\rho} = \rho_r \exp(z' Di / \gamma_r), \text{ and } \bar{T} = \frac{T_{\text{surf}}}{\Delta T_r} \exp(z' Di), \quad (17)$$

where z' is the dimensionless vertical coordinate. The conservation of energy (12) under the ALA becomes,

$$\bar{\rho} c_p \frac{DT'}{Dt} + Di \bar{\rho} \bar{\alpha} w T' = \nabla^2 T' + \bar{\rho} H + \phi \frac{Di}{Ra} + Di^2 \bar{T}. \quad (18)$$

Eq. (18) resembles the familiar energy equation in Boussinesq convection with the addition of three terms: the viscous dissipation, $\phi \frac{Di}{Ra}$, the work done against gravity,

$$W = Di \bar{\rho} \bar{\alpha} w T', \quad (19)$$

and a second-order term in dissipation number, $Di^2 \bar{T}$ that arises from substituting eq. (17) into the $\nabla \cdot (k \nabla \bar{T})$ term in eq. (12). Because \bar{T} is independent of time and only depends on depth, this term acts like a depth-dependent internal heat source. The volume-averaged work done against gravity $\langle W \rangle$ exactly balances the volume-averaged viscous dissipation $\langle \phi \rangle$ (Hewitt *et al.* 1975; Zhang & Yuen 1996; Leng & Zhong 2008). This is one of the measures that we use to assess the energy conservation of the codes.

2.1.1 Boundary conditions for compressible convection

It is important to point out that boundary conditions for temperature require special care when compared with the more commonly used Boussinesq approximation. In the description here, the total temperature jump across the model is ΔT_r which is comprised of both a contribution from the reference state \bar{T} and the potential temperature T' . The non-dimensional temperature at the surface, T_o is given by $T_{\text{surf}} / \Delta T_r$. Because eq. (18) is written in terms of the potential temperature, T' the boundary conditions for eq. (18) are, $T'(z = 0) = 0$ and $T'(z = 1) = 1 - \exp(Di)$. This requires care when defining the Nusselt number, as discussed below. The different codes used different formulations (e.g. CU formulation is based on total temperature, while the VT and UM formulations are based on potential temperature). Assessing whether or not this impacted the results from these codes was one of the objectives of the benchmark project.

It is also worth pointing out that the reference state used here fails when $T_o \rightarrow 0$, leading to the non-sensible reference temperature state $\bar{T} = 0$. For the ALA benchmark, eqs (14), (15) and (18) are solved.

2.2 Equations under the truncated anelastic liquid approximation (TALA)

For the TALA, the pressure term in the buoyancy force is ignored, in which case eq. (15) becomes

$$0 = -\nabla p' + \nabla \cdot \tau - Ra \bar{\rho} \bar{\alpha} \hat{g} T'. \quad (20)$$

Some numerical methods have difficulty with eq. (15) and the TALA (eq. 20) has often been used in compressible studies (Jarvis & McKenzie 1980; Christensen & Yuen 1985; Ita & King 1994). Jarvis & McKenzie (1980) show that there is an imbalance between viscous dissipation and gravitational potential energy with the TALA. Leng & Zhong (2008) demonstrate that the imbalance is caused by ignoring the effect of dynamic pressure on buoyancy and

can be removed using the ALA. We further compare the difference between these formulations below.

2.3 Equations under the extended Boussinesq approximation (EBA)

For the EBA, the reference state changes to $\bar{\rho} = 1$ and $\bar{T} = 0$. This leads to the first step beyond the Boussinesq approximation and is a useful check that the additional terms in the energy equation that scale with dissipation number, Di , have been implemented and scale properly. With the further assumption that $\bar{\alpha} = 1$, $k = 1$ and $c_{pr} = 1$, the conservation and constitutive equations become,

$$\nabla \cdot \bar{u} = 0, \quad (21)$$

the conservation of momentum becomes,

$$0 = -\nabla p + \nabla \cdot \tau - Ra \hat{g} T' \quad (22)$$

$$\frac{DT'}{Dt} + Di w (T' + T_o) = \nabla^2 T' + \bar{\rho} H + \phi \frac{Di}{Ra}. \quad (23)$$

and

$$\tau = 2\eta \dot{\epsilon} = \eta (\nabla \bar{u} + \nabla \bar{u}^T). \quad (24)$$

Note that because $\bar{T} = 0$, the boundary condition at the base of the fluid layer remains unmodified in the EBA (i.e. $T' = 1$).

2.4 Equations under the Boussinesq approximation (BA)

By dropping the terms that scale with the dissipation number, Di , eqs (21)–(23) reduce to the Boussinesq approximation. Under the BA, eqs (21), (22) and (24) remain unchanged and eq. (23) becomes

$$\frac{DT'}{Dt} = \nabla^2 T' + \bar{\rho} H. \quad (25)$$

3 DESCRIPTION OF THE BENCHMARK PROBLEMS

The benchmark problems are an extension of the problems in the Blankenbach *et al.* (1989) benchmark. **We begin with a unit-aspect ratio domain, with free-slip top, bottom, and sides walls.** The total temperature is fixed at the top $T(z = 0) = 0$ and bottom $T(z = 1) = 1$ and the side-walls have no flux boundary conditions. **We consider BA, EBA, TALA and ALA.** All thermodynamic properties are fixed constants. The Rayleigh number, Ra , ranges from 10^4 to 10^6 and we vary the Dissipation number, Di , from 0 to 2. For the initial cases, we consider a constant viscosity fluid. Each participant selected the grid that was best suited to their method. All grids used in the benchmark are in the range of 60–128 elements (or nodes) per side. We compared some solutions on more refined grids to check the convergence of the methods and error; however, the grids here are sufficient to resolve the problems in this study. The participants were asked to report surface heat flux (Nusselt number) and rms velocity for all cases and in addition, the viscous dissipation and work done for the compressible cases.

The Nusselt number is a ratio of the average surface heat flow from the convective solution to the heat flow due to conduction and is calculated by,

$$Nu = -\frac{1}{\lambda \Delta T} \int_0^\lambda \frac{\partial T'(x, z = z_{\text{top}})}{\partial z} dx, \quad (26)$$

where 0 and λ are the left- and right-hand coordinates of the domain, respectively, z_{top} is the top of the domain and, ΔT is the temperature contrast across the domain. The rms velocity is given by

$$V_{\text{rms}} = \frac{1}{\lambda(z_{\text{top}} - z_{\text{bot}})} \int_{z_{\text{bot}}}^{z_{\text{top}}} \int_0^\lambda [(u^2 + w^2)]^{\frac{1}{2}} dx dz. \quad (27)$$

In addition to the set of calculations described above, we added a series of temperature-dependent cases with a viscosity function,

$$\eta(T) = \eta_0 \exp[-\beta T], \quad (28)$$

where $\eta_0 = 1$, T is normalized by $\Delta T = 3000$ and $\beta = \ln(1000)$, following problem 2a in Blankenbach *et al.* (1989). These calculations are in a unit-aspect ratio domain, with free-slip top, bottom and sides walls. Participants were asked to provide ALA results if possible and if not, TALA results.

For the time-dependent cases we focus on the transition from steady to the first time-dependent mode for the case with a dissipation number of 0.25 for constant viscosity convection in the unit-aspect ratio domain, with free-slip top, bottom and sides walls. Time-dependent behaviour in the unit-aspect ratio domain occurs at lower Rayleigh numbers for compressible convection than incompressible convection. As this problem appears to be sensitive to the initial condition, we suggested that participants start from the steady solution for the Rayleigh number 5×10^5 , dissipation number 0.25 case, for which all participants found a steady one-cell solution. Participants were asked to provide ALA results if possible and if not, TALA results.

4 DESCRIPTION OF THE CODES

Most of the codes here are based on incompressible versions that have been described in detail elsewhere. The description of the codes here focuses on the modifications for compressible convection. For the reader's convenience we have provided Table 1 with a short description of solution techniques and mesh resolution used. A more complete description is provided below.

Van Keken from the University of Michigan (UM) provided a code based on the finite element package *Sepran* used in van Keken *et al.* (2002). Streamline-upwind Petrov–Galerkin elements (Hughes & Brooks 1979; Hughes *et al.* 1988) are used for energy equation, which is solved with a Picard iteration scheme (with a relaxation factor, typically 0.5) to achieve steady-state solutions. Taylor–Hood elements (Taylor & Hood P. 1973) are used in the momentum equation. Both the energy and momentum equations are solved iteratively with Bi-CGstab and ILU pre-conditioner. For the benchmark problems a mesh consisting of 60×68 elements with

refinement in top and bottom boundary layers is used, except for the time-dependent problem.

King and Lee from Virginia Tech (VT) provided a code based on the finite element code *ConMan* (King *et al.* 1990) with the compressible formulation described in Lee & King (2009). Streamline-upwind Petrov–Galerkin elements (Hughes & Brooks 1979; Hughes *et al.* 1988) as implemented in the original *ConMan* solver are used for the energy equation with a second-order predictor–corrector method for time stepping or Picard iteration. A penalty method (Hughes *et al.* 1979) is used to eliminate pressure in the momentum equation and we consider two different direct solution methods: a non-symmetric direct solver and the original symmetric Cholesky solver in *ConMan*, where we move the non-symmetric terms to the right-hand side of the equation and iterate, as in Ita & King (1994). We found for the TALA results, both the symmetric plus right-hand side terms and non-symmetric solver produced identical results, whereas we found putting the non-symmetric terms on the right-hand side would not converge for the ALA formulation. For the benchmark problems a mesh consisting of 64 square elements on each side is used.

Leng and Zhong from University of Colorado (CU) provided a code based on the finite element code *Citcom* (Moresi *et al.* 1996) with the compressible formulation described in Leng & Zhong (2008). Streamline-upwind Petrov–Galerkin elements (Hughes & Brooks 1979; Hughes *et al.* 1988) are used for energy equation, which is solved with a second-order predictor–corrector method for time stepping. The momentum equation is solved by a modified Uzawa algorithm (Cahouet & Cahbard 1988). For the benchmark problems a mesh consisting of 64 elements on each side with refinement in top and bottom thermal boundary layers are used.

Tan from Caltech (CT) provided a code the finite element code *Citcom* (Moresi *et al.* 1996) with the compressible formulation described in Tan & Gurnis (2005, 2007). Streamline-upwind Petrov–Galerkin elements (Hughes & Brooks 1979; Hughes *et al.* 1988) are used for energy equation, which is solved with a second-order predictor–corrector method for time stepping. An Uzawa scheme for the momentum eq. (Cahouet & Cahbard 1988) with the outer loop (correcting pressure) solved with Bi-CGstab and the inner loop (solving velocity for given pressure) is solved with LU decomposition. W is computed at element level while the ϕ is computed on the node level because the stresses can be oscillatory in the elements (*cf.* Hughes 1987). For the benchmark problems a mesh consisting of 64 square elements on each side are used.

Tosi from Charles University (CZ) provided a code where the equations are discretized using a control volume representation. For each cell of the domain, the momentum equation is first solved for horizontal and vertical velocity at staggered nodes, then the continuity equation is explicitly solved for the pressure at the centre

Table 1. Summary of methods and discretizations for the codes used in the benchmark.

Code	Energy equation	Energy discretization	Momentum equation	Momentum discretization	Benchmark mesh
UM (Sepran)	Picard	SUPG	BI-CGStab/ILU	Taylor-Hood	$60 \times 68r$
VT (ConMan)	Picard	SUPG	Penalty/direct	Q1-P0	64×64
CT (ConMan)	2nd-order explicit	SUPG	Uzawa/Bi-CGStab/LU	Q1-P0	64×64
CU (Citcom)	2nd-order explicit	SUPG	Uzawa/multigrid	Q1-P0	$64 \times 64r$
CZ	Semi-Lagrangian Crank-Nicolson	Finite volume	direct	Finite volume	$70 \times 70r$
KS	Crank-Nicolson or implicit	First-order Euler FD with upwinding	Artificial compressibility/ multigrid	Finite volume	128×128

Notes: SUPG is Streamline-Upwind Petrov Galerkin elements. BI-CGStab is stabilized bidirectional conjugate gradient method. ILU is incomplete LU factorization. Q1-P0 are linear velocity constant pressure elements. An r after the grid values indicates top and bottom refinement of the grid. Complete code descriptions are given in the text and associated references.

of the cell (Gerya & Yuen 2003). For the energy equation a semi-Lagrangian operator splitting method is used (Spiegelman & Katz 2006). The temperature is first advected through a semi-Lagrangian scheme with bicubic interpolation. Then, a Crank-Nicolson scheme is employed to diffuse the advected temperature. Both linear systems are solved using the parallel direct sparse solver PARDISO (Schenk *et al.* 2000). For the benchmark problems a mesh consisting of a 70×70 staggered grid with refinement in the top and bottom thermal boundary layers is used.

Kameyama from Ehime University (KS) provided a code that solves eqs (14)–(18) under the assumption that $\tilde{T} = 0$ with a **finite volume discretization**. The Stokes equation is solved for primitive variables (velocity and pressure) by the multigrid method together with the smoothing algorithm based on the artificial compressibility and local time-stepping techniques (Kameyama *et al.* 2005). The energy equation is discretized by a first-order Euler method in time. An upwind scheme, called the power-law scheme (Patankar 1980), is used to evaluate the contributions of heat transport by advection and conduction. The discretized equation is solved by a fully implicit scheme when we seek for a steady-state convection, or by the Crank–Nicolson scheme when we seek for a time-dependent convection. For the benchmark problems a mesh consisting of a 128×128 uniformly spaced nodes is used.

5 RESULTS

We begin by illustrating the agreement of the codes using the BA, eqs (21), (22), (25) and (24). The difference between the Nu (eq. 26) and rms-velocity (eq. 27) for the six codes from a high-resolution (256×256 element grid) VT calculation for the steady-state, BA cases for Rayleigh numbers 10^4 – 10^6 is shown in Fig. 1. The high resolution VT results ($Ra = 10^6$, $Nu = 21.9765$, rms-velocity = 834.20) agree quite well with the extrapolated results of Christensen ($Ra = 10^6$, $Nu = 21.9720$, rms-Velocity = 833.99) reported in Blankenbach *et al.* (1989). All of the codes produce a steady, one cell solution and all results are in excellent agreement up to a Rayleigh number of 2×10^5 . Above a Rayleigh number of 2×10^5 , the difference between the high-resolution VT result and the UM, CU, CZ and KS codes becomes systematically larger with the CU, KS and UM results in close agreement with each other. Yet even for a Rayleigh number of 10^6 the largest difference in Nusselt number is

less than 1 per cent for the CU, KS and UM codes and slightly larger for the CZ code. For the rms-velocity the UM is almost identical to the high-resolution VT result while the CU, CT and low-resolution VT results cluster together slightly higher than the high-resolution VT result, the CZ result is larger still, and the KS result is slightly lower than the high-resolution VT result. The KS rms-velocities are almost identical to the high-resolution VT results for all the other cases and the Rayleigh number 10^6 result could still be approaching the steady-state solution. The compressible solutions are less vigorous and thus these grids are sufficient to resolve the solutions that follow. The VT and UM solutions use Picard iteration to find the steady-state solution quickly, while the other codes explicitly integrate forward in time until a steady-solution is achieved. The data for all calculations are available in the online supplement Table 1.

We next address the calculation of the viscous dissipation, ϕ , and the work against the gravitational potential, W , by considering the EBA, eqs (21), (22), (23) and (24). To highlight the differences between the codes, we plot the difference between the Nusselt number and rms velocity relative to the 64×64 element VT calculation. The Nu difference, rms-velocity difference, viscous dissipation (eq. 5) and work (eq. 19) for the six codes for the steady-state, EBA cases for Rayleigh numbers 10^4 – 10^6 are shown in Figs 2–4 for $Di = 0.25$, 0.5 and 1.0, respectively. We plot total magnitude of viscous dissipation (eq. 5) and work (eq. 19), as opposed to relative differences to illustrate the level of agreement among the codes. All codes found steady, one-cell flows up to a Rayleigh number of 5×10^6 for dissipation numbers 0.25 and 0.5. For $Di = 0.25$ at Rayleigh numbers of 5×10^5 and 10^6 several of the codes found steady two-cell solutions. Due to the inherent non-linearity of the equations it is sometimes difficult to attain a one-cell steady state starting from a conductive solution and in general the contributors obtained the higher Rayleigh number solutions by starting from the steady solution at a lower Rayleigh number. It is interesting note that none of the solutions at high Di show penetrative convection. This style of convection, where the lower part of the model are stabilized by a steep adiabatic gradient, was reported by Jarvis & McKenzie (1980), but this is likely due to the flux boundary condition that was used in that paper, rather than the fixed temperature boundary condition employed here.

The VT code has the largest Nusselt number and rms-velocity for all Rayleigh numbers for the dissipation number of 0.25 and

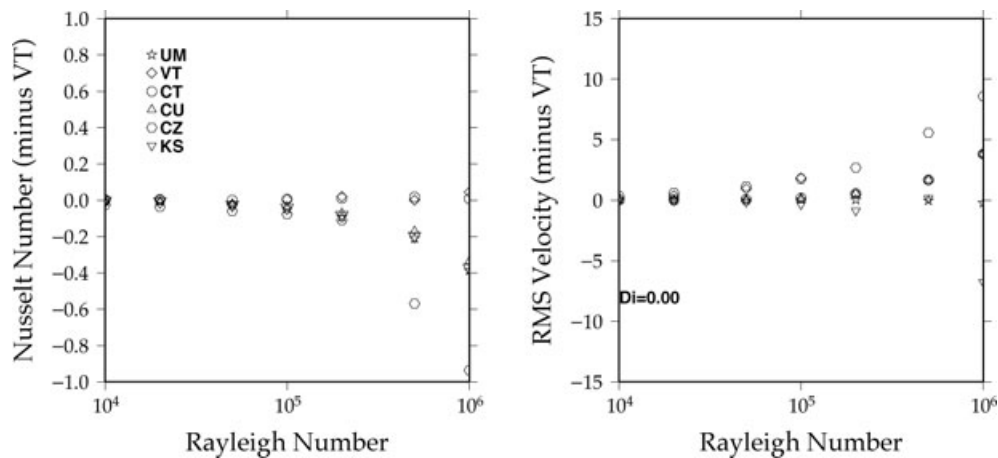


Figure 1. Nusselt number (eq. 26) and rms-velocity (eq. 27) for the six codes subtracted from a high resolution (256×256 element grid) VT calculation for the steady-state, Boussinesq Approximation (BA) cases for Rayleigh numbers 10^4 – 10^6 . In this and following figures we identify the codes by an acronym identifying (approximately) the originating institution: UM - University of Michigan; VT - Virginia Tech; CT - Caltech; CU - University of Colorado at Boulder; CZ - Charles University in Prague and KS - Ehime University.

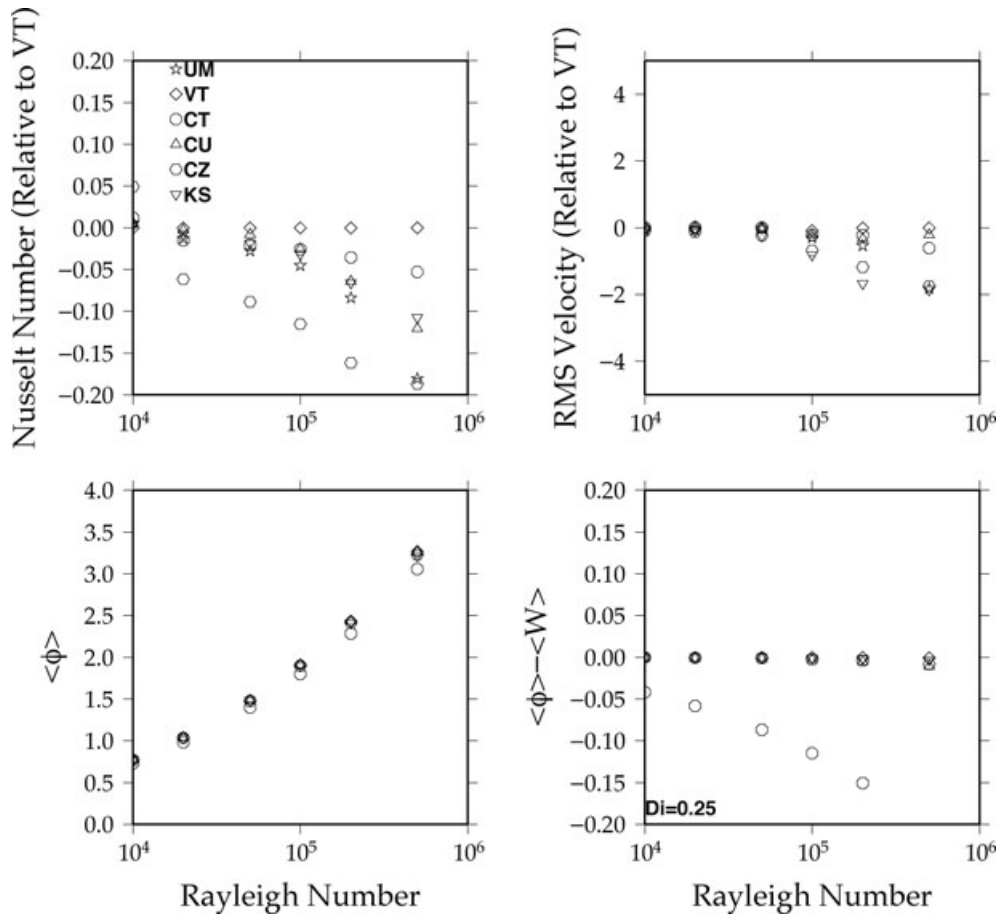


Figure 2. Nusselt number and rms-velocity differences subtracted from 64×64 element VT result, viscous dissipation (eq. 5) and work (eq. 19) for the six codes for the steady-state, Extended Boussinesq Approximation (EBA) cases for Rayleigh numbers 10^4 – 10^6 with $Di = 0.25$. The codes are identified by an acronym based on (approximately) the originating institution. See Fig. 1.

0.5 (below Rayleigh number of 5×10^5) and the CZ code had the smallest Nusselt number and rms-velocity over the same range. The differences between codes grow systematically as a function of Rayleigh number and decreases with increasing dissipation number. The magnitude of the difference is similar to the magnitude of the difference between the BA results and the high-resolution VT code and shows similar behaviour with Rayleigh number. We observe occasional systematic differences in Nu and V_{rms} . These are likely due to consistent differences in discretization (resolution as well as the use of finite volume versus finite elements) or differences in the treatment of the incompressibility constraint. Since the differences are small we have not performed a systematic study to investigate the causes suggesting that the difference is related to resolution. This is less than a 1 per cent difference in rms velocity and somewhat larger difference in Nusselt number and follows a similar trend with the difference between the UM and high-resolution VT solution in Fig. 1. The other notable disagreement among the results is for the calculation of ϕ and the difference between ϕ and W for the CT code. This results because the calculation of ϕ is done at the element level while the calculation of W is done at the node level and is a post-processing issue that does not impact the solution, as the agreement between the Nusselt number and rms velocity demonstrates. The data for all calculations are available in Tables S2–S4.

Next we compare the TALA results using eqs (14), (20), (18) and (3). Nu (eq. 26), rms-velocity (eq. 27), viscous dissipation (eq. 5) and work (eq. 19) for the six codes for the steady-state, TALA cases

for Rayleigh numbers 10^4 – 10^6 are shown in Figs 5 and 6 for $Di = 0.25$ and 1.0. Nusselt number and rms-velocity are plotted relative to the VT solution to highlight the differences. All of the solutions are steady, one-cell flows. We see a similar pattern to the EBA results with the VT code producing the largest Nusselt number and rms-velocity for all Rayleigh numbers and the CZ code produces the smallest Nusselt number while KS produces the smallest rms-velocity. The difference between the largest and smallest values grows with increasing Rayleigh number and the magnitude of the difference is similar to the magnitude of the difference between the codes and high-resolution VT results for the Boussinesq cases. For the $Di = 0.25$ cases, the balance between viscous dissipation, ϕ and the integral of work done against gravity, W , are nearly in balance, except for the CT code where the post-processing problem is again apparent. For the $Di = 1$ cases (Fig. 6), the difference between results is smaller. This again suggests that grid resolution differences dominate the difference between the codes because for the $Di = 1.0$ cases the vigour of convection is reduced. This is more apparent by looking at the Nusselt number and rms-velocity as a function of dissipation number for the Rayleigh number 10^5 case (Fig. 7). Here the absolute values of Nusselt number and rms-velocity are plotted. The largest discrepancy between the results from different codes is for $Di = 1.25$ where some codes report a single cell solution and other codes report two cell solutions. The imbalance between work and viscous dissipation grows until the dissipation number reaches 1.25 and then decreases. The decrease

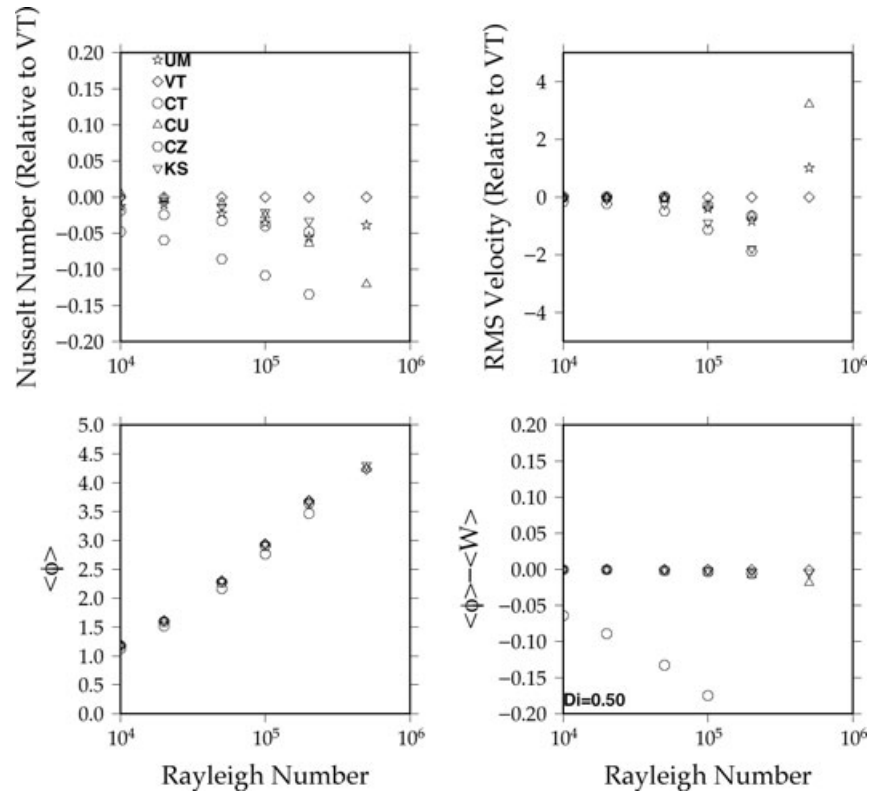


Figure 3. Nusselt number and rms-velocity differences subtracted from 64×64 element VT result, viscous dissipation (eq. 5) and work (eq. 19) for the six codes for the steady-state, EBA cases for Rayleigh numbers 10^4 – 10^6 with $Di = 0.5$. The codes are identified by an acronym based on (approximately) the originating institution. See Fig. 1.

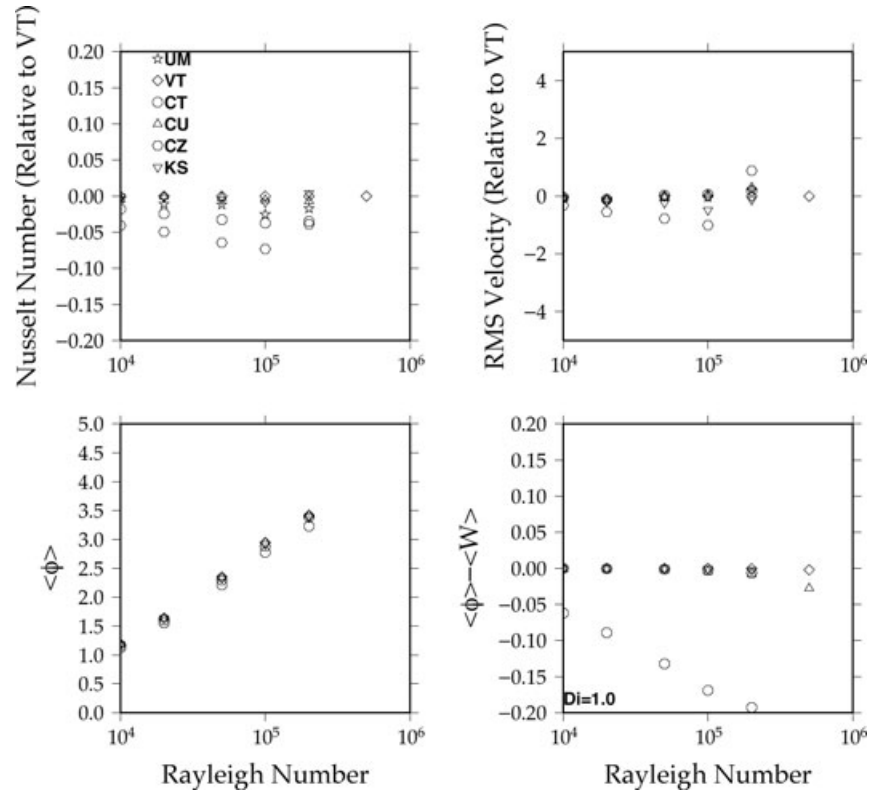


Figure 4. Nusselt number and rms-velocity differences subtracted from 64×64 element VT result, viscous dissipation (eq. 5) and work (eq. 19) for the six codes for the steady-state, EBA cases for Rayleigh numbers 10^4 – 10^6 with $Di = 1.00$. The codes are identified by an acronym based on (approximately) the originating institution. See Fig. 1.

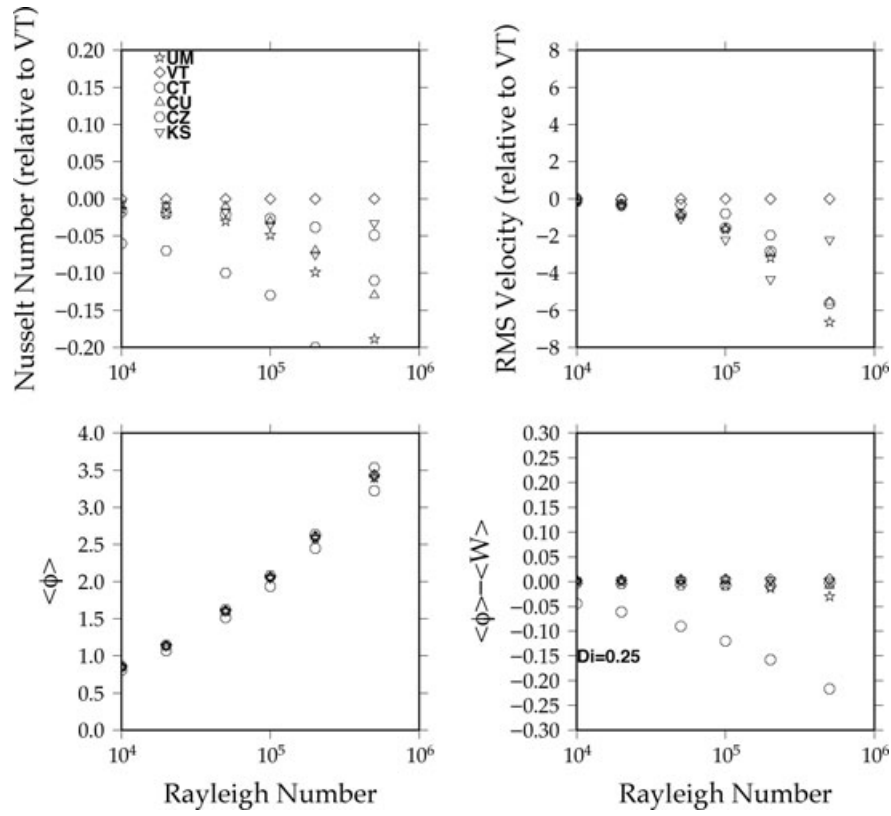


Figure 5. Nusselt number and rms-velocity differences subtracted from 64×64 element VT result, viscous dissipation (eq. 5) and work (eq. 19) for the six codes for the steady-state, truncated anelastic liquid approximation (TALA) cases for Rayleigh numbers 10^4 – 10^6 with $Di = 0.25$.

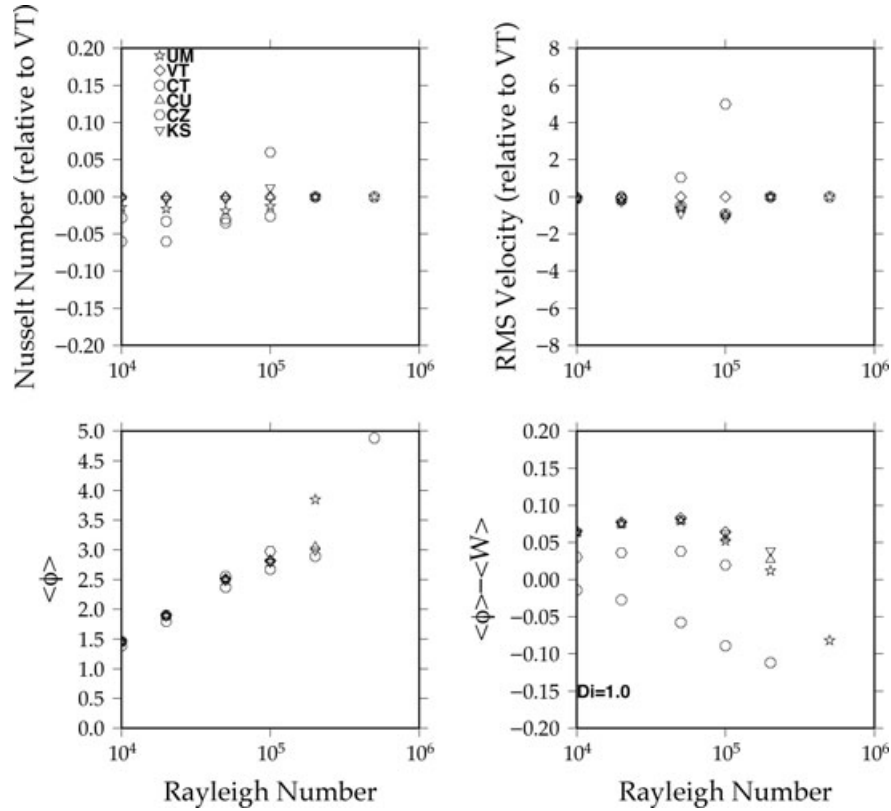


Figure 6. Nusselt number and rms-velocity differences subtracted from 64×64 element VT result, viscous dissipation (eq. 5) and work (eq. 19) for the six codes for the steady-state, TALA cases for Rayleigh numbers 10^4 – 10^6 with $Di = 1.00$.

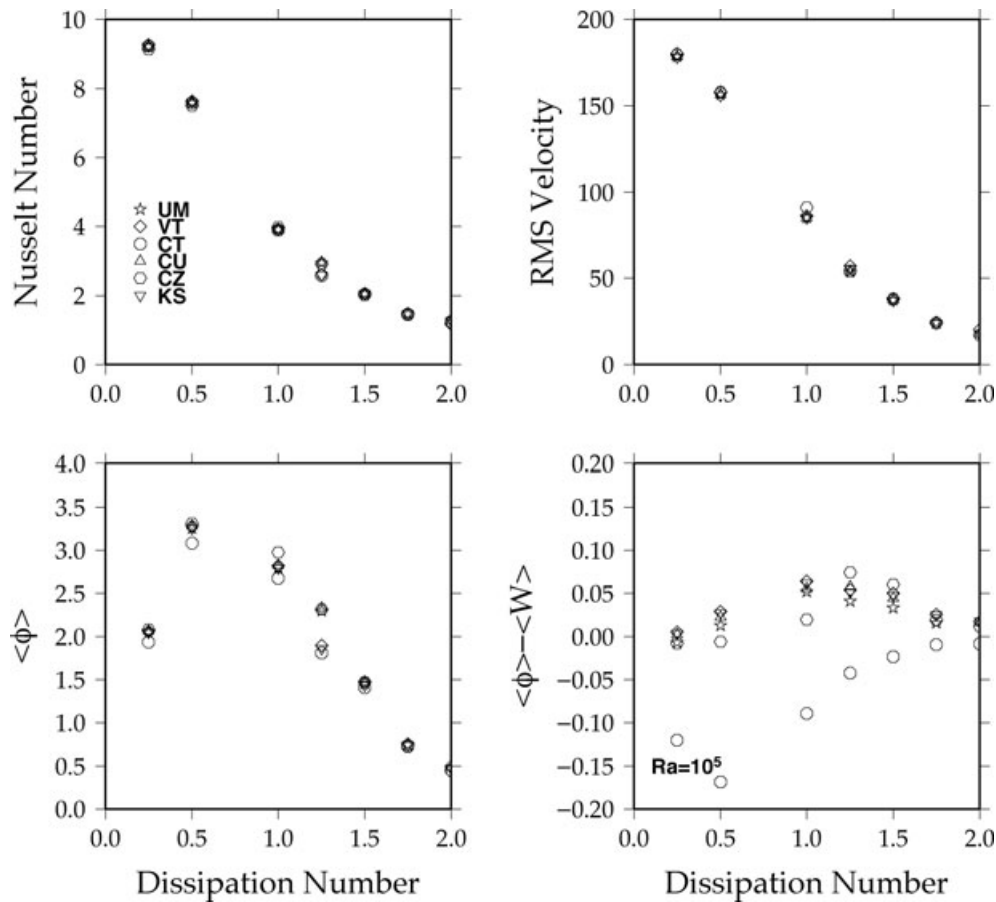


Figure 7. Nusselt number and rms-velocity, viscous dissipation (eq. 5) and work (eq. 19) for the six codes for the steady-state, TALA cases for Rayleigh number 10^5 with $Di = 0 - 2$.

occurs because the total amount of work decreases as the vigour of convection increases. The results for the TALA calculations from $Di = 0.25-2$ for all six codes are available in Table S5–S11.

Finally we compare the ALA results using eqs (14), (15), (18) and (3). Nu (eq. 26), rms-velocity (eq. 27), viscous dissipation (eq. 5) and work (eq. 19) for the three codes for the steady-state, ALA cases for Rayleigh numbers 10^4-10^6 are shown in Figs 8 and 9 for $Di = 0.25$ and 1.0. Only three codes had an ALA formulation (UM, VT and CU) however the results were consistent with all previous results, VT produced the largest Nusselt number and rms-velocity and UM produced the smallest (with the exception of $Ra = 5 \times 10^5$) and the trend was increasing difference with increasing Rayleigh number. Once again, the differences between the code are on the same order as the differences due to resolution. The VT code produced the best balance of work and gravitational potential energy, with the UM and CU code showing a slight imbalance that appears to increase with increasing Rayleigh number. All of the solutions are steady, one-cell flows for dissipation number of 0.25 and for the lower Rayleigh numbers at dissipation number 1.0. For dissipation number 1.0 and Rayleigh number 2×10^5 the UM code found a steady two cell solution while CU and VT found a single-cell solution. All codes found a steady two-cell solution for dissipation number 1.0 and Rayleigh number 5×10^5 . The results as a function of dissipation number (Fig. 10) parallel the TALA results with the exception of the balance between viscous dissipation and work, which is uniformly closer to zero for the ALA cases regardless of dissipation number.

The results for the ALA calculations from $Di = 0.25-2$ for VT, UM and CU are available in Table S12–S15.

The results plotted in the figures are obtained with grids consisting of 60–70 nodes (elements) in each direction except for KS which used 128 nodes in each direction. For some cases, authors reported convergence tests. The grids used are noted in the online supplemental tables. For consistency, each code used the same grid for all results plotted in the figures except for the time-dependent results as noted in that section. To demonstrate typical convergence, we show the results of a grid resolution study from then VT code using 32, 64, 96 and 128 uniformly spaced elements in each direction for the TALA problem described above with a Rayleigh number of 10^4 and dissipation numbers of 0.25, 0.5 and 1.0 (Fig. 11). The difference between the Nusselt number and rms-velocity on the 32×32 and 128×128 grids differs by less than 1 per cent. For the codes using grid refinement, the results may converge faster when compared with the uniform grids used by the VT code. The results for the convergence study with the VT code are available in Table S16.

5.1 Difference between TALA and ALA results

Because the ALA formulation requires an accurate calculation of the dynamic pressure, some codes are unable to solve the equations under the ALA and are limited to the TALA. To evaluate the difference between ALA and TALA results, we plot the difference between the calculated Nusselt number and rms-velocity from codes using the ALA and TALA formulation, plotting the difference

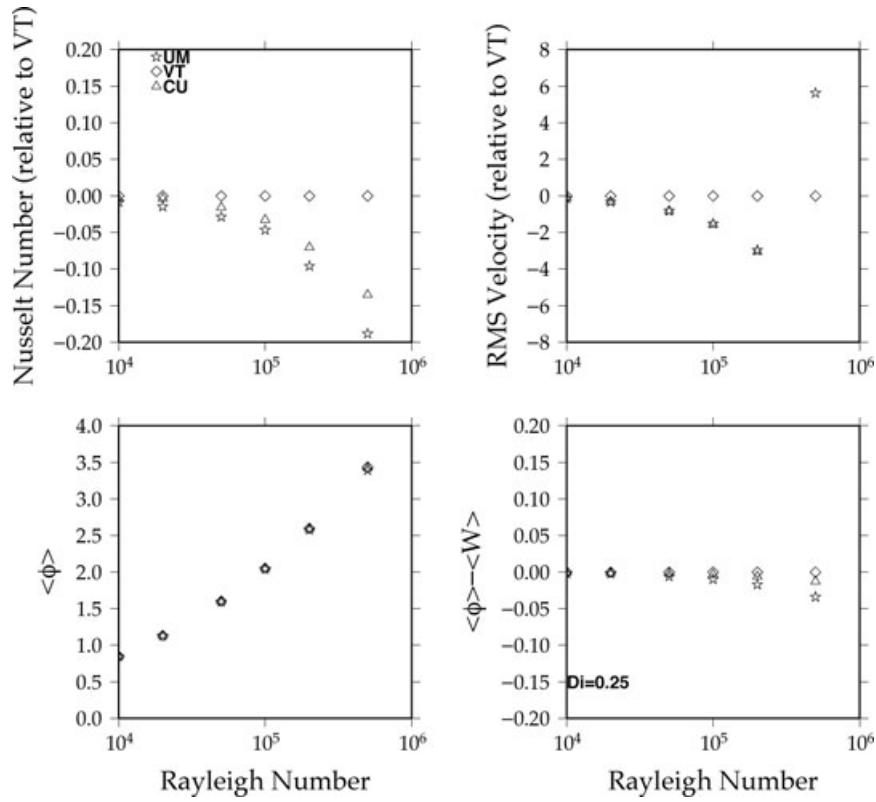


Figure 8. Nusselt number and rms-velocity differences subtracted from 64×64 element VT result, viscous dissipation (eq. 5) and work (eq. 19) for the UM, CU and VT codes for the steady-state, anelastic liquid approximation (ALA) cases for Rayleigh numbers 10^4 – 10^6 with $Di = 0.25$.

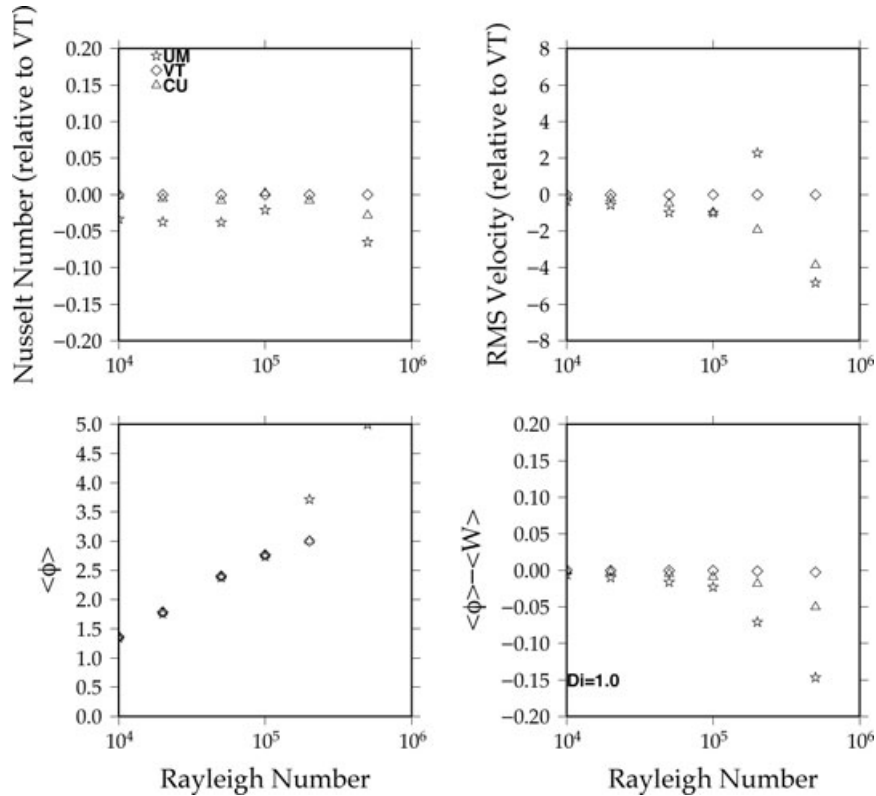


Figure 9. Nusselt number and rms-velocity differences subtracted from 64×64 element VT result, viscous dissipation (eq. 5) and work (eq. 19) for the UM, CU and VT codes for the steady-state, ALA cases for Rayleigh numbers 10^4 – 10^6 with $Di = 1.00$.

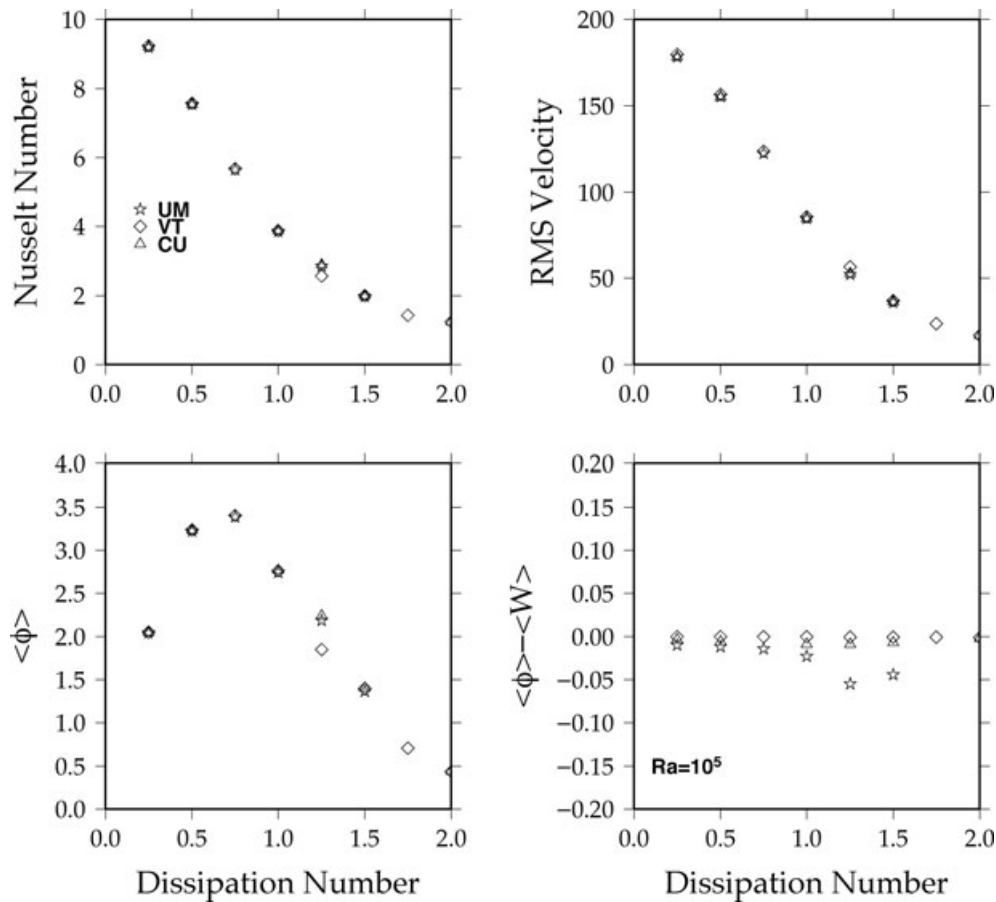


Figure 10. Nusselt number and rms-velocity, viscous dissipation (eq. 5) and work (eq. 19) for the UM, CU and VT codes for the steady-state cases for Rayleigh number 10^5 with $Di = 0 - 2$.

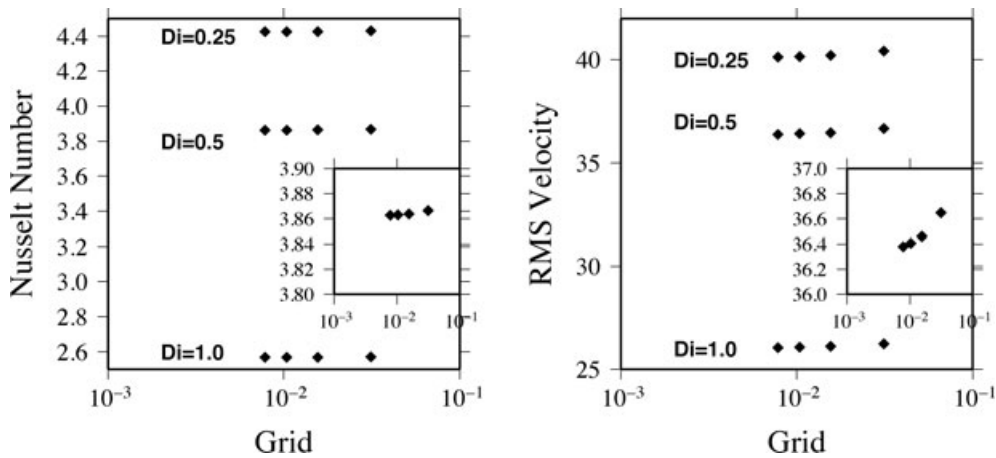


Figure 11. Nusselt number and rms-velocity as a function of grid spacing for TALA calculations using the VT code with Rayleigh number 10^5 and dissipation number 0.25, 0.5 and 1.0. The inset figures focus in on the dissipation number 0.5 cases.

between results obtained from the same code using the same grid for each approximation. As seen in Figs 12–14, the difference between the ALA and TALA is slightly larger than the grid resolution errors for the dissipation numbers 0.5 and 1.0 cases and the codes behave consistently as a function of both Rayleigh number and dissipation

number. The differences between the ALA and TALA results grow systematically larger (although small) as the dissipation number increases and, with the exception of the Nusselt number from the CU code for the $Di = 0.25$ cases, show little systematic variation with Rayleigh number. While previous work (Jarvis & McKenzie

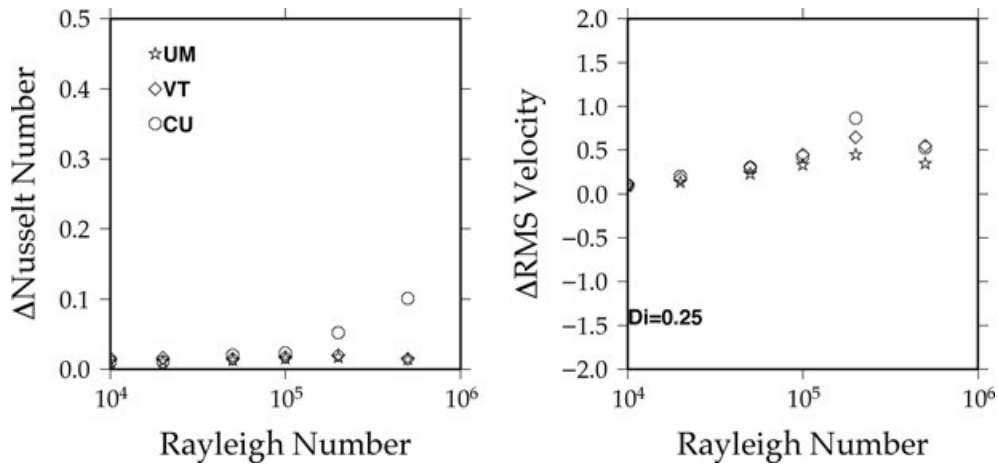


Figure 12. Nusselt number and rms-velocity differences between the ALA and TALA formulation from the UM, CU and VT codes for the steady-state cases with Rayleigh numbers 10^4 – 10^6 with $Di = 0.25$. The systematic differences reflect the energy imbalance in the truncated anelastic liquid approximation.

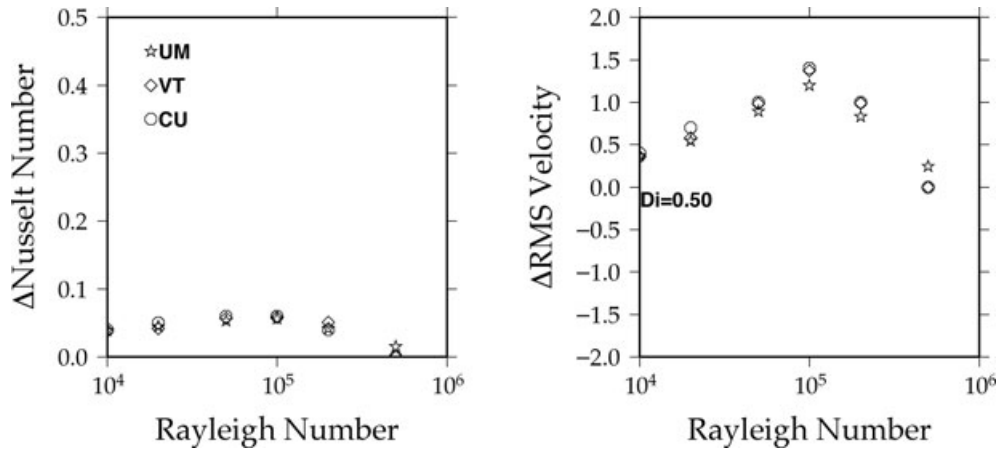


Figure 13. Nusselt number (eq. 26), rms-velocity (eq. 27) differences between the ALA and TALA formulation from the UM, CU and VT codes for the steady-state cases with Rayleigh numbers 10^4 – 10^6 with $Di = 0.50$.

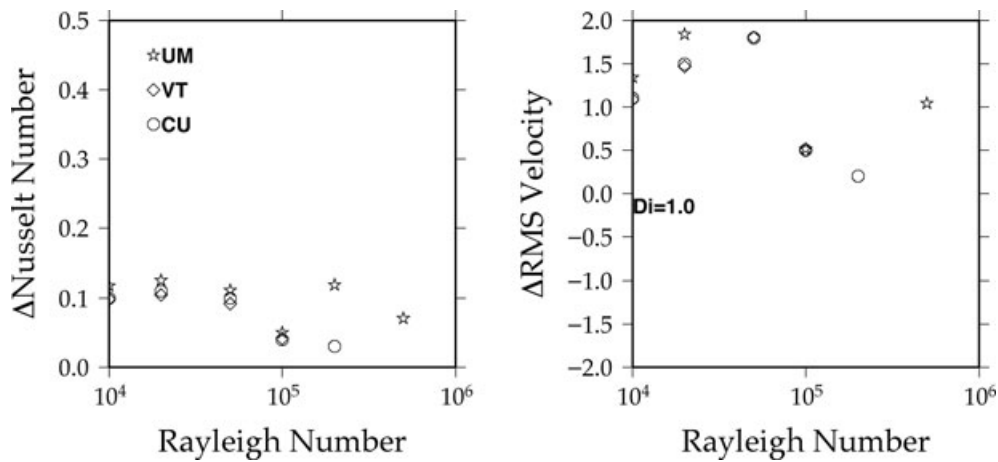


Figure 14. Nusselt number (eq. 26), rms-velocity (eq. 27) differences between the ALA and TALA formulation from the UM, CU and VT codes for the steady-state cases with Rayleigh numbers 10^4 – 10^6 with $Di = 1.00$.

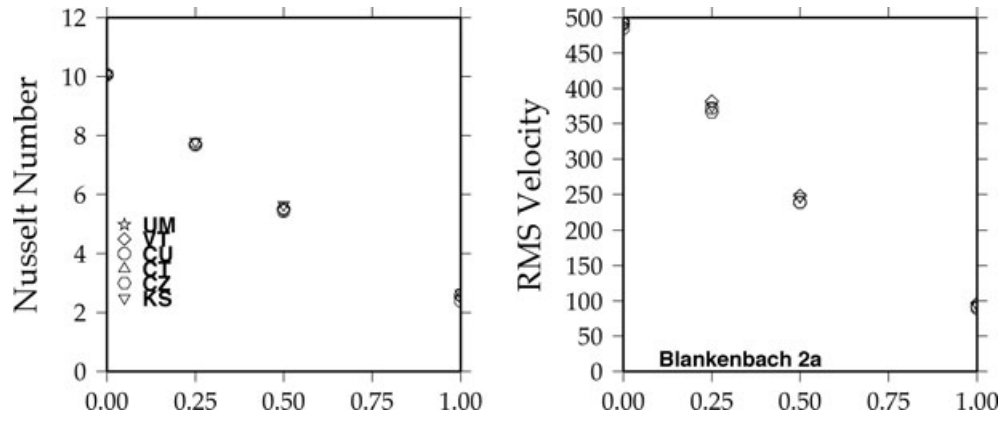


Figure 15. Nusselt number (eq. 26), rms-velocity (eq. 27) for the six codes for the steady-state cases with temperature-dependent viscosity using ALA (UM, VT, CU) or TALA (CT, CZ, KS) for Rayleigh number 10^4 with $Di = 0.25$ – 2 . This is a compressible equivalent of case 2a of the Blankenbach *et al.*, 1989 benchmark.

1980) has shown that the TALA results in a systematic imbalance in the conservation of energy and that energy is conserved using ALA (Leng & Zhong 2008), the results here show that for dissipation numbers of order 0.25, the difference between the TALA and ALA is of the same order as the difference between codes and only slightly larger than the level of grid resolution errors. However, the difference grows with increasing dissipation number in the TALA formulation (Fig. 7) and is quite significant for $Di = 0.75$ – 1.25 for many codes.

5.2 Temperature-dependent viscosity results

We compare ALA (or TALA) results for convection in the same domain using the temperature-dependent rheology described in eq. (28). The Nu (eq. 26), rms-velocity (eq. 27), viscous dissipation (eq. 5) and work (eq. 19) for the six codes for the steady-state, ALA (or TALA) are shown in Fig. 15 for a Rayleigh number of 10^4 and dissipation numbers from 0–2. The case with $Di = 0$ corresponds to case 2a in the Blankenbach *et al.* (1989). The absolute Nusselt number and rms-velocity are plotted. The difference between the solutions is similar in magnitude and pattern to the difference among the constant viscosity solutions. All of the solutions are steady, one-cell flows and once again for several of the codes it was necessary to coax the solution into the steady, one-cell flow at the higher Rayleigh numbers by starting from the steady solution at a lower Rayleigh number. The results for the temperature-dependent calculations for all six code are available in Table S17.

5.3 Time-dependent convection results

As the compressible formulations lead to time-dependent behaviour in the unit-aspect ratio domain at lower Rayleigh numbers than incompressible convection, we decided to test whether the different codes obtain the same time-dependent behaviour. To confirm that the time-dependent algorithms worked correctly for the Boussinesq case, we first requested the results for case 3 from the Blankenbach *et al.* (1989) benchmark. This Boussinesq benchmark is for an aspect ratio 1.5 domain that is internally heated with an isothermal top, zero-heat flux bottom and side boundaries. The top and bottom boundaries are rigid and side walls have reflective boundary conditions. The Rayleigh number of the Blankenbach case is 216 000. In this problem, the fluid shows a regular oscillatory behaviour where instabilities in the top boundary layer are formed and are swept into the downwelling. At first, every blob is identical (P1 cycle), then at slightly higher Rayleigh numbers every second blob is identical (P2 cycle), then every fourth (P4 cycle). Most codes in the Blankenbach study found a P2 cycle at this Rayleigh number and reported maximum and minimum Nusselt numbers and rms-velocities along with the period of the oscillation. All of our codes produced a P2 cycle at this Rayleigh number and the results are reported in Table 2.

For the compressible time-dependent case we focus on the Rayleigh number where the transition to time-dependence first occurs in aspect ratio one case with constant viscosity and $Di = 0.25$. Participants reported the maximum and minimum Nusselt number, rms-velocity, period and character of the instability at the Rayleigh numbers around the transition. UM, CU and VT use 128×128 refined grids for the time-dependent problem and found that lower

Table 2. Comparison of incompressible time-dependent results with Blankenbach *et al.* (1989) case 3.

Code	Resolution	$Nu_{\max 1}$	$Nu_{\min 1}$	$Nu_{\max 2}$	$Nu_{\min 2}$	$Vr_{\max 1}$	$Vr_{\min 1}$	$Vr_{\max 2}$	$Vr_{\min 2}$	Period
UM	$90 \times 68r$	7.360	6.462	7.178	6.773	60.630	31.939	57.81	30.36	0.04805
UM	$160 \times 128r$	7.378	6.468	7.201	6.797	60.479	31.949	57.633	30.316	0.04812
VT	$94 \times 64r$	7.392	6.482	7.218	6.796	60.329	31.831	57.477	30.222	0.04840
VT	$192 \times 128r$	7.382	6.472	7.201	6.796	60.575	31.961	57.712	30.346	0.04840
CU	$128 \times 128r$	7.381	6.468	7.199	6.796	60.427	32.005	57.466	30.332	0.04824
CZ	$100 \times 70r$	7.359	6.441	7.185	6.770	60.536	31.987	57.734	30.329	0.04900
CT	$192 \times 136r$	7.424	6.506	7.236	6.841	60.42	30.32	57.45	32.13	0.0481
KS	192×128	7.379	6.472	7.199	6.797	60.296	31.988	57.416	30.344	0.04810
BB best		7.379	6.468	7.196	6.796	60.367	31.981	57.43	30.32	0.04803

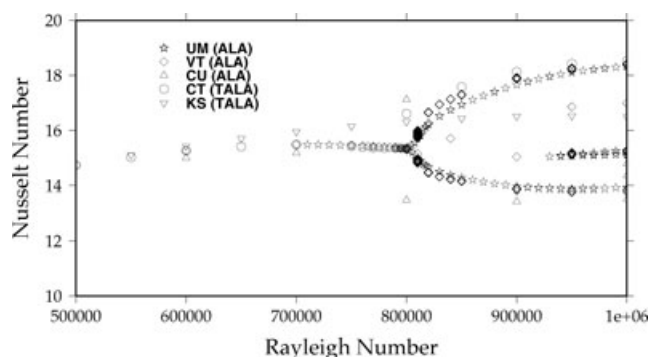


Figure 16. Nusselt number (eq. 26) as a function of Rayleigh number for constant viscosity ALA (UM, VT, CU) or TALA (CT, KS) calculations with $Di = 0.25$. The transition from steady state to periodic convection is a classical bifurcation in a non-linear system. Due to the sudden transition it provides an important test for the accuracy of the time-integration methods, particularly for compressible convection where the inherent non-linearities are stronger than in the case of Boussinesq convection. UM, VT and CU find the transition to time-dependent convection in a Rayleigh number range of $7.79\text{--}8.0 \times 10^5$, CZ finds steady-state solutions up to 9×10^5 while KS finds steady solutions up to 1.05×10^6 .

resolution grids give somewhat inconsistent results. The results from the UM, VT, CZ and KS are plotted in Fig. 16. UM, VT and CU use ALA find the transition to time-dependent convection within a Rayleigh number range of $7.79\text{--}8.0 \times 10^5$, while CZ and KS, both using TALA, find steady-state solutions up to 9×10^5 and 1.05×10^6 , respectively. All codes report an initial P1 mode of time-dependence, while some codes found an additional transition to P2 with a small increase in Rayleigh number beyond the initial transition.

6 CONCLUSIONS

Our benchmark comparison shows a satisfactory agreement among all codes for most of the quantities for all compressible formulations. The differences between codes for a given problem are generally the same magnitude as the grid resolution errors between the code and a high-resolution solution for Boussinesq convection. Although we did not perform a grid resolution study for all compressible cases, the consistency of the pattern of the results as a function of Rayleigh number regardless of compressible approximation suggests that grid errors dominate the differences between codes. We find a small but systematic difference between TALA and ALA results that is only weakly dependent on Rayleigh number. This difference is only slightly larger than the differences due to grid resolution. **The results for temperature-dependent, steady convection are consistent with the constant viscosity results and suggest that the interaction between rheology and viscous dissipation is something that all methods were able to handle.** In compressible convection the transition to time-dependent behaviour in the unit-aspect-ratio domain occurs at a lower Rayleigh number than incompressible convection. This is perhaps not surprising given that a number of the codes found two-cell solutions at Rayleigh numbers where steady, one-cell solutions are found in incompressible convection. It appears that the most unstable wavelengths of compressible convection are smaller than for incompressible convection.

ACKNOWLEDGMENTS

We thank Magali Billen and an anonymous reviewer for their constructive comments. We thank CIG for support of the 2006 compressible convection workshop. We also acknowledge support from NSF-IF-0317638 and NSF-EAR-0749708. N. Tosi acknowledges support from the European Commission through the Marie Curie Research Training Network ‘C2C’ (contract MRTN-CT-2006-035957).

REFERENCES

- Birch, F., 1952. Elasticity and constitution of the Earth's interior, *J. geophys. Res.*, **57**, 227–286.
- Blankenbach, B. *et al.*, 1989. A benchmark comparison for mantle convection codes, *Geophys. J. Int.*, **98**, 23–38.
- Cahouet, C. & Cabbard, J.-P., 1988. Some fast 3D finite element solvers for the generalized Stokes' problem, *Int. J. Numer. Methods Fluids*, **8**, 869–895.
- Christensen, U.R. & Yuen, D.A., 1985. Layered convection induced by phase transitions, *J. geophys. Res.*, **90**, 10 291–10 300.
- Gerya, T. & Yuen, D.A., 2003. Characteristic-based marker-in-cell method with conservative finite-differences schemes for modelling geological flows with strongly variable transport properties, *Phys. Earth planet. Inter.*, **140**, 293–318.
- Hewitt, J.M., McKenzie, D.P. & Weiss, N.O., 1975. Dissipative heating in convective flows, *J. Fluid Mech.*, **68**, 721–738.
- Hughes, T.J.R., 1987. *The Finite Element Method*. Prentice-Hall, Inc., Englewood Cliffs, NJ.
- Hughes, T.J.R. & Brooks, A.N., 1979. A multi-dimensional upwind scheme with no crosswind diffusion, in *Finite Element Methods for Convection Dominated Flows*, Vol. 34, pp. 19–35, ed. Hughes, T.J.R., ASME, New York.
- Hughes, T.J.R., Liu, W.K. & Brooks, A.N., 1979. Finite element analysis of incompressible viscous flows by the penalty function formulation. *J. Comput. Phys.*, **30**, 1–60.
- Hughes, T.J.R., Franca, L.P. & Hulbert, G.M., Johan, Z. & Shakib, F., 1988. The Galerkin/least-squares method for advective-diffusive equations, in *Recent Developments in Computational Fluid Dynamics*, Vol. 95, pp. 75–99, ed. Tezduyar, T.E., ASME, New York.
- Ita, J. & King, S.D., 1994. Sensitivity of convection with an endothermic phase-change to the form of governing equations, initial conditions, boundary conditions, and equation of state, *J. geophys. Res.*, **99**(B8), 15 919–15 938.
- Ita, J.J. & King, S.D., 1998. The influence of thermodynamic formulation on simulations of subduction zone geometry and history, *Geophys. Res. Lett.*, **125**, 1463–1466.
- Jarvis, G.T. & McKenzie, D.P., 1980. Convection in a compressible fluid with infinite Prandtl number, *J. Fluid Mech.*, **96**, 515–583.
- Kameyama, M., Kageyama, A. & Sato, T., 2005. Multigrid iterative algorithm using pseudo-compressibility for three-dimensional mantle convection with strongly variable viscosity, *J. Comp. Phys.*, **206**, 162–181.
- King, S.D., 2009. On topography and geoid from 2D stagnant-lid convection calculations, *Geochem. Geophys. Geosys.*, **10**, Q3002, doi:10.1029/2008GC002250.
- King, S.D. & Ita, J.J., 1995. The effect of slab rheology on mass transport across a phase transition boundary, *J. geophys. Res.*, **100**, 20 211–20 222.
- King, S.D., Raefsky, A. & Hager, B.H., 1990. Conman: Vectorizing a finite-element code for incompressible 2-dimensional convection in the Earth's mantle, *Phys. Earth planet. Inter.*, **59**, 195–208.
- Koglin, D.E. Jr., Ghias, S., King, S.D., Jarvis, G.T. & Lowman, J.P., 2005. Mantle convection with mobile plates: a benchmark study, *Geochem. Geophys. Geosyst.*, **6**, Q09003, doi:10.1029/2005GC000924.
- Lee, C. & King, S.D., 2009. The effect of mantle compressibility on the thermal and flow structures of the subduction zone, *Geochem. Geophys. Geosyst.*, **10**, Q1006, doi:10.1029/2008GC002151.

- Leng, W. & Zhong, S., 2008. Viscous heating, adiabatic heating and energetic consistency in compressible mantle convection, *Geophys. J. Int.*, **173**, 693–702.
- Moresi, L., Zhong, S.J. & Gurnis, M., 1996. The accuracy of finite element solutions of Stokes' flow with strongly varying viscosity, *Phys. Earth planet. Inter.*, **97**, 83–94.
- Patankar, S.V., 1980. *Numerical Heat Transfer and Fluid Flow*, McGraw-Hill, New York.
- Schenk, O., Gartner, K. & Fichtner, W., 2000. Efficient sparse LU factorization with left-right looking strategy on shared memory multiprocessors, *BIT*, **40**(1), 158–176.
- Schubert, G., Turcotte, D.L. & Olson, P., 2001. *Mantle Convection in the Earth and Planets*, 940 pp., Cambridge Univ. Press, New York.
- Spiegelman, M. & Katz, R., 2006. A semi-Lagrangian Crank-Nicolson algorithm for the numerical solution of advection-diffusion problems, *Geochem. Geophys. Geosys.*, **7**, Q04014, doi:10.1029/2005GC001073.
- Tan, E. & Gurnis, M., 2005. Metastable superplumes and mantle compressibility, *Geophys. Res. Lett.*, **32**, L20307, doi:10.1029/2005GL024190.
- Tan, E. & Gurnis, M., 2007. Compressible thermochemical convection and application to lower mantle structures, *J. geophys. Res.*, **112**, B06304, doi:10.1029/2006JB004505.
- Taylor, C. & Hood P., 1973. A numerical solution of the Navier-Stokes equations using the finite element technique, *Comput. Fluids*, **1**, 73–100.
- Travis, B.J. *et al.*, 1990. A benchmark comparison of numerical methods for infinite Prandtl number thermal convection in two-dimensional Cartesian geometry, *Geophys. Astrophys. Fluid Dyn.*, **55**, 137–160.
- Turcotte, D.L., Hsui, A.T., Torrance, K.E. & Schubert, G., 1974. Influence of viscous dissipation on Benard convection, *J. Fluid Mech.*, **64**, 369–374.
- van Keken, P.E., King, S.D., Schmeling, H., Christensen, U.R., Neumeister, D. & Doin, M.-P., 1997. A comparison of methods for the modeling of thermochemical convection, *J. geophys. Res.*, **102**, 22 477–22 495.
- van Keken, P.E., Kiefer, B. & Peacock, S., 2002. High resolution models of subduction zones: implications for mineral dehydration reactions and the transport of water into the deep mantle, *Geochem. Geophys. Geosys.*, **3**(10), 1056, doi:10.1029/2001GC000256.
- van Keken, P.E. *et al.*, 2008. A community benchmark for subduction zone modeling, *Phys. Earth planet. Inter.*, **171**, 187–197.
- Yuen, D.A., Quarení, F. & Hong, H.J., 1987. Effects from equation of state and rheology in dissipative heating in compressible mantle convection, *Nature*, **326**, 67–69.
- Zhang, S. & Yuen, D.A., 1996. Various influences on plumes and dynamics in time-dependent, compressible mantle convection in 3-D spherical shell, *Phys. Earth planet. Inter.*, **94**, 241–267.

SUPPORTING INFORMATION

Additional Supporting Information may be found in the online version of this article:

Tables S1–S17. Tables of computational model output corresponding to the figures in this paper.

Please note: Wiley-Blackwell are not responsible for the content or functionality of any supporting materials supplied by the authors. Any queries (other than missing material) should be directed to the corresponding author for the article.